

Peer Review The peer review history for this article is available as a PDF in the Supporting Information.

Key Points:

- Seismic velocity, density, and basalt content at and below the 660-km discontinuity (d660) are constrained by *S660S* waveform inversions
- Slabs exhibit a smaller impedance jump across the d660 but a steeper gradient below the d660 compared to other regions
- Basalt accumulates at the d660, especially in subduction zones, but decreases significantly below it, forming a harzburgite-enriched layer

Supporting Information:

Supporting Information may be found in the online version of this article.

Correspondence to:

S. Hao,
s2hao@ucsd.edu

Citation:

Hao, S., Wei, S. S., & Shearer, P. M. (2024). Substantial global radial variations of basalt content near the 660-km discontinuity. *AGU Advances*, 5, e2024AV001409. <https://doi.org/10.1029/2024AV001409>

Received 15 JUL 2024

Accepted 28 OCT 2024

Author Contributions:

Conceptualization: Shangqin Hao,

S. Shawn Wei, Peter M. Shearer

Data curation: Shangqin Hao

Formal analysis: Shangqin Hao

Funding acquisition: Peter M. Shearer

Investigation: Shangqin Hao, Peter

M. Shearer

Methodology: Shangqin Hao,

S. Shawn Wei, Peter M. Shearer

Project administration: Peter M. Shearer

Resources: Shangqin Hao, S. Shawn Wei, Peter M. Shearer

© 2024. The Author(s).

This is an open access article under the terms of the [Creative Commons](#)

[Attribution-NonCommercial-NoDerivs](#)

License, which permits use and distribution in any medium, provided the original work is properly cited, the use is non-commercial and no modifications or adaptations are made.

Substantial Global Radial Variations of Basalt Content Near the 660-km Discontinuity

Shangqin Hao¹ , S. Shawn Wei² , and Peter M. Shearer¹ 

¹Institute of Geophysics and Planetary Physics, Scripps Institution of Oceanography, UC San Diego, La Jolla, CA, USA,

²Department of Earth and Environmental Sciences, Michigan State University, East Lansing, MI, USA

Abstract Mid-ocean ridges generate basalt and harzburgite, which are introduced into the mantle through subduction as a mechanical mixture, contributing to both lateral and radial compositional heterogeneity. The possible accumulation of basalt in the mantle transition zone has been examined, but details of the mantle composition below the 660-km discontinuity (hereafter d660) remain poorly constrained. In this study, we utilize the subtle waveform details of *S660S*, the underside shear-wave reflection off the d660, to interpret the seismic velocity, density, and compositional structure near, and particularly below, the d660. We identify a significant difference in *S660S* waveform shape in subduction zones compared to other regions. The inversion results reveal globally enriched basalt at the d660, with a notably higher content in subduction zones, consistent with the smaller impedance jump and *S660S* peak amplitude. The basalt fraction decreases significantly to less than 10% near 800-km depth, forming a global harzburgite-enriched layer and resulting in a steep seismic velocity gradient just below the d660, in agreement with 1D global reference models. The striking compositional radial variations near the d660 verify geodynamic predictions and challenge the applicability of homogeneous radial compositional models in the mantle. These variations may also affect the viscosity profile and, consequently, the dynamics at the boundary between the upper and lower mantle.

Plain Language Summary Compositional heterogeneity is prevalent in Earth's mantle. The basalt and harzburgite generated by mid-ocean ridges are transported by subducted slabs into the deep mantle, but they do not reach chemical equilibrium over geological time scales. Therefore, the heterogeneous mantle can be modeled as a physical mixture of varying amounts of these two components. Basalt can separate from slabs and be transported elsewhere, but its spatial distribution is poorly known, which is crucial for understanding the mantle's composition and evolution. The 660-km discontinuity (d660) is the boundary between the upper and lower mantle. This study fully utilizes the subtle details of the seismic wave *S660S*, the underside shear-wave reflection off the d660, to resolve the basalt content at and below the d660. Our results show that basalt accumulates at the d660, particularly in subduction zones, consistent with previous studies. However, the basalt fraction decreases substantially below the d660, producing a global harzburgite-enriched layer, which may influence the dynamics between the upper and lower mantle. Integrating our findings with mineral physics and geochemical constraints provides a more detailed understanding of the radial variations in mantle chemistry.

1. Introduction

Compositional heterogeneity is prevalent throughout the mantle, varying across different scales and heavily influenced by mantle convection and plate tectonics (e.g., Stixrude & Lithgow-Bertelloni, 2012, and references therein). The mantle is processed at mid-ocean ridges, generating basaltic magma and depleted harzburgitic residue, which are then injected into the deep mantle through subduction. Because of the low chemical diffusivity of mantle materials (Farber et al., 1994; Hofmann & Hart, 1978; Yamazaki et al., 2000), harzburgite and basalt are not likely to reach equilibrium over the age of the Earth. Therefore, in contrast to widely used homogeneous models, such as the pyrolite model (Ringwood, 1962), a mechanical mixture of basalt and harzburgite is more likely to represent the mantle composition (e.g., Xu et al., 2008). Due to the greater depth of the gradual post-garnet transition than that of the post-spinel transition, basalt is denser than harzburgite throughout the entire mantle, except at depths of about 660–720 km (Hirose et al., 1999; Ishii et al., 2019; W. Wang, Xu, et al., 2020). The density crossover, according to numerical experiments and geodynamic modeling (Van Keken et al., 1996; Yan et al., 2020), should result in a basalt-enriched layer in the mantle transition zone (MTZ) and a harzburgite-enriched layer at depths of approximately 660–800 km, which has been observed in some regions, such as the Samoan mantle plume (Maguire et al., 2017). If this prediction is valid, the 660-km discontinuity (hereafter d660)

Software: Shangqin Hao, Peter M. Shearer
Supervision: S. Shawn Wei, Peter M. Shearer
Validation: Shangqin Hao
Visualization: Shangqin Hao
Writing – original draft: Shangqin Hao
Writing – review & editing: Shangqin Hao, S. Shawn Wei, Peter M. Shearer

would be not only a phase boundary but also a compositional boundary between the upper and lower mantle, producing radial compositional variations that could influence mantle dynamics.

Owing to the distinct seismic velocity and density properties of basalt and harzburgite, particularly near the d660, seismological approaches provide an opportunity to resolve compositional mantle heterogeneity. The reflected seismic waves at discontinuities that arrive before the main *PP* and *SS* phases, named *PP* and *SS* precursors, respectively, provide good global coverage and are widely used in studying the MTZ discontinuities. Recently, some seismological studies confirmed the global accumulation of basalt in the MTZ by analyzing *PP* and *SS* precursors reflected at the 410-km discontinuity (hereafter d410) and d660 (Bissig et al., 2023; Tauzin et al., 2022; Yu et al., 2023). These results also suggest a higher basalt fraction at the d660 compared to the d410, with an increased presence near subduction slabs than in other regions. Although there is a discrepancy in the absolute basalt content in these studies due to differences in methods and uncertainties in mineral databases, a general consensus has been reached on the basalt-enriched layer above the d660. However, the seismic velocity, density, and composition immediately below the d660 remain poorly constrained, presenting a critical challenge in assessing the possible existence of a distinct compositional layer between the upper and lower mantle.

To resolve structure below the d660, we examine details of the underside reflected phase *S660S*. Prior *PP* and *SS* precursor studies typically rely on travel time and peak amplitude to infer the topography and velocity/density changes across discontinuities. However, waveform characteristics, including sidelobes (secondary waveform details surrounding the main peak) (Figure 1f), offer additional valuable information, particularly concerning the velocity/density gradient near discontinuities. For example, the deep right sidelobe of *S410S* in some regions may be the signature of a low-velocity layer above the d410 (Wei & Shearer, 2017). An interesting feature near the d660 is the steep seismic velocity gradient below it in 1D global reference models (e.g., Dziewonski & Anderson, 1981; Kennett & Engdahl, 1991), which accounts for the shallow sidelobe on the left side of a global *S660S* stack by Shearer (1996). Thus, the waveform details of *S660S* provide a chance to resolve the fine velocity structure not only at but also above and below the d660. In this study, using more than 30 years of global seismic data, we identify a significant difference in *S660S* waveform shape between subducting slabs and other regions. We interpret these results with inversions for seismic velocity models alone and for models that incorporate mineral physics constraints for compositional models of varying basalt content. Our results provide new constraints on radial compositional variations near the d660, which can be integrated with previous seismic and geochemical findings and incorporated into geodynamic modeling to enhance our understanding of Earth's composition and evolution.

2. Data and Methods

2.1. Data Processing and Stacking

We utilize the large data set of *SS* precursors compiled in Wei et al. (2020), comprising seismic data recorded at global permanent broadband stations, USArray stations, and Japan F-net stations from 1987 to 2018. To reduce interference from depth phases, only events shallower than 75-km depth are included. Each transverse-component seismogram is band-pass filtered between 15 and 100 s (first-order Butterworth, zero-phase shift) and subsequently downsampled to 1 s. The *SS* phase is picked as the maximum absolute amplitude in a 60-s time window centered at the theoretical *SS* arrival time predicted by the IASP91 model (Kennett & Engdahl, 1991). The noise is estimated from the maximum amplitude in a time window from 50 s before the predicted *S660S* arrival to 50 s after the predicted *S410S* arrival. To ensure high data quality and avoid potential interference from the *Ss660s* and *ScS660ScS* phases, we only retain seismograms with *SS* signal-to-noise ratios greater than 3 and source-receiver distances within the range of 120 to 170°. This screening process results in a total of 143,059 traces and each trace is aligned and normalized to the *SS* arrival.

To mitigate the effect of the uneven data distribution, the traces are stacked in overlapping caps of 5° radius at a spacing of 5° based on their bounce points (Figure 1). Cap stacks containing fewer than 100 bounce points are discarded due to their high stacking error. *SS* stacks are obtained by directly stacking traces along the *SS* arrival, whereas *S660S* stacks are obtained by stacking traces along the predicted *S660S* arrival time relative to *SS*, accounting for lateral velocity variations. Following the approach of Shearer (1993), we utilized the CRUST1.0 model (Laske et al., 2013) and the GLAD-M25 model (Lei et al., 2020) to generate 1D S-wave velocity profiles for each trace and compute the theoretical differential travel time between *SS* and *S660S* ($t_{SS} - t_{S660S}$). The *S660S* cap stacks are further aligned to the maximum amplitude within the time window from −10 to 10 s relative to the

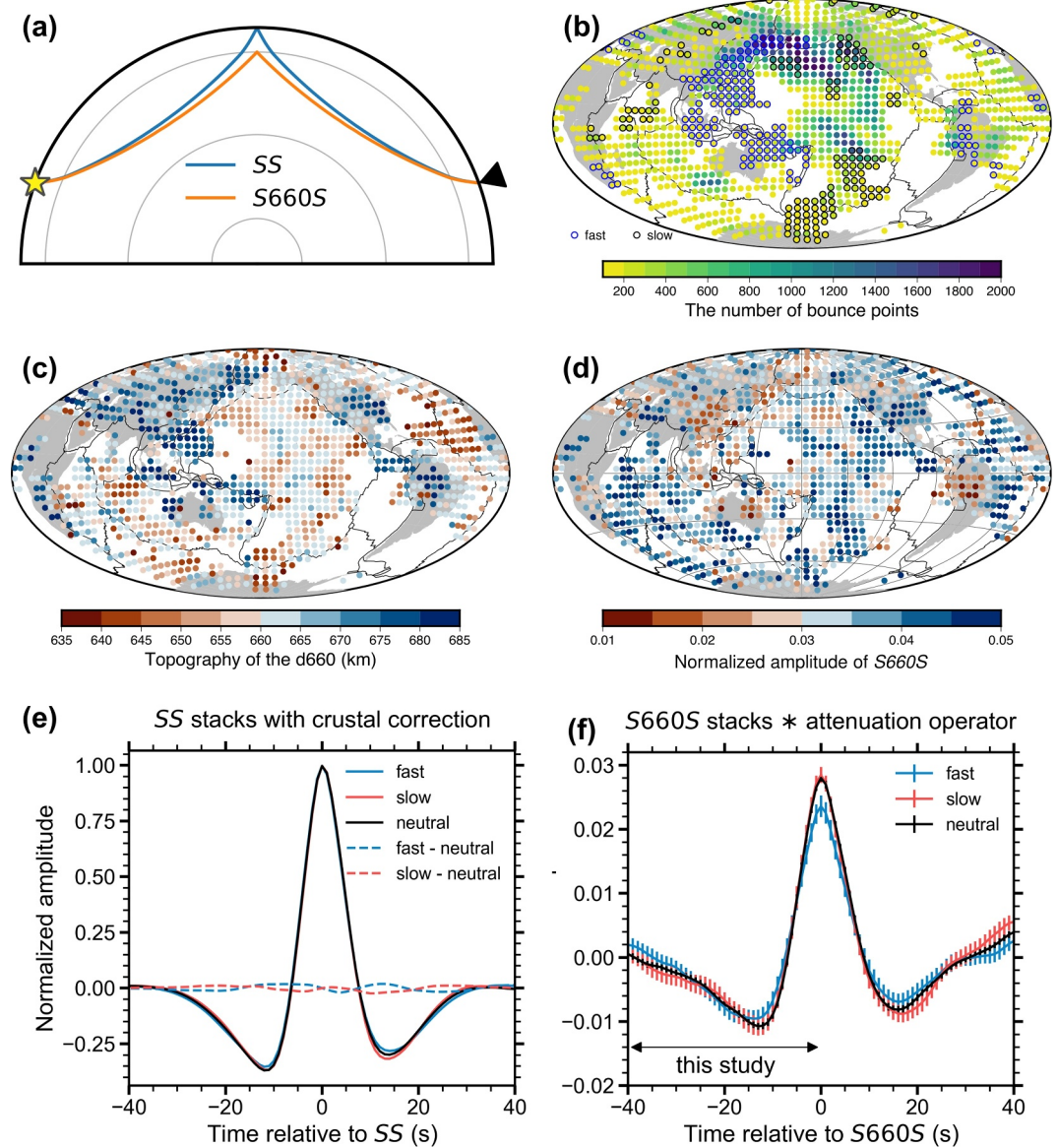


Figure 1. *S660S* data and stacks. (a) Ray paths of *SS* and *S660S* at a representative epicentral distance of 140° , where the star and triangle represent the earthquake and station, respectively. (b) Distribution of fast, slow, and neutral caps containing more than 100 bounce points. The fast and slow caps are delineated with blue and black edges, respectively. The plotting size of the caps is smaller than the real radius of 5° to avoid overlapping. (c) Topography of the *d660* in caps with more than 100 bounce points. (d) Normalized amplitude of *S660S* in caps with more than 100 bounce points. The black lines in panels (b–d) represent the plate boundary. (e, f) Corrected *SS* and *S660S* stacks in fast, slow, and neutral groups. The *SS* stacks are corrected for variations in crustal thickness and the *S660S* stacks represent the convolution of the original *S660S* stacks and an attenuation operator, accounting for the additional attenuation of *SS* compared to *S660S*. Two-standard error bars are shown in panel (f), which are estimated using the bootstrapping approach (Efron & Tibshirani, 1991).

predicted *S660S* arrival and the travel time deviations from the prediction are converted to the topography of the *d660* (Figure 1c) (see details in Section 3.1).

To characterize possible structural and compositional differences between subduction zones, hot upwelling, and ambient mantle, we divide the caps into three groups based on global tomography models. The vote maps of absolute velocities exceeding the root-mean-square velocity at the depth of 660 km from 18 global S-wave tomography models are generated using SubMachine (Hosseini et al., 2018; Shephard et al., 2017) (Figure S1 in Supporting Information S1). Caps in regions with at least 9 votes, representing half of the models, are classified as

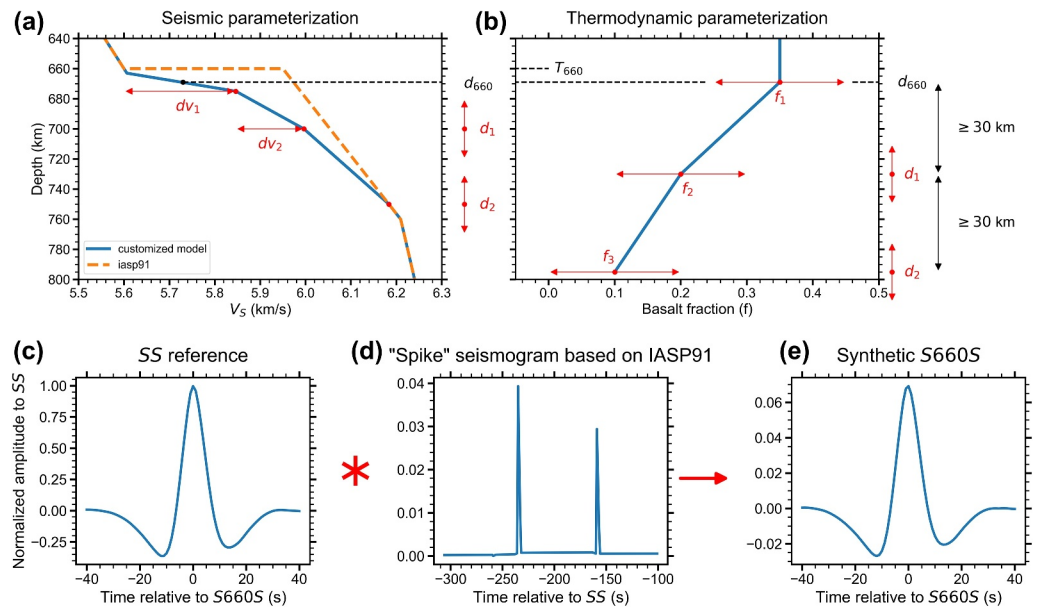


Figure 2. Parameterizations and waveform modeling. (a, b) Illustration of parameters in the seismic and thermodynamic parameterizations. Free parameters are highlighted in red, whereas the d_{660} depth (d_{660}) is fixed and estimated by the timing of *S660S*. (c–e) The waveform modeling approach illustrated using the IASP91 model as an example. The synthetic *S660S* waveform is the convolution of the reference *SS* and a “spike” seismogram calculated based on the 1D model. The reference *SS* phase is corrected for effects of the crust and the synthetic *S660S* is compared with the observed *S660S* after accounting for attenuation, as shown in Figures 1e and 1f.

fast or slow caps depending on the polarity of their velocity anomalies. The remaining caps are designated as neutral caps (Figure 1b). In each group, all the aligned cap stacks are further stacked to generate the *SS* and *S660S* group stacks (Figures 1e and 1f), with the uncertainty in the *S660S* stacks estimated using the bootstrapping approach (Efron & Tibshirani, 1991). The three sets of group stacks, named fast, slow, and neutral stacks, generally correspond to regions of cold subducted slab, hot upwelling, and ambient mantle, as temperature is the predominant factor controlling the lateral changes in seismic velocity.

2.2. Waveform Modeling

Based on ray theory and a given 1D model, a synthetic *S660S* waveform can be efficiently computed by convolving the reference *SS* waveform with the discontinuity operator calculated from reflection coefficients and geometric spreading (Lawrence & Shearer, 2006; Shearer, 1996) (Figures 2c–2e). The epicentral distances used in this study avoid triplications, caustics, and diffracted waves, making ray theory a suitable approximation for the forward problem. Given this method to generate synthetic waveforms, the 1D profile beneath a region (e.g., the fast region), can be inverted for using the corresponding *SS* and *S660S* data stacks. Note that the *SS* stack for each group is utilized as the reference phase for the corresponding *S660S* stack.

The weighted average epicentral distance of the global data set, 140° , is used as a representative distance to calculate the synthetics, and tests show negligible differences between the group stacks of traces with different epicentral distances and the synthetic based on 140° (Figure S2 in Supporting Information S1). To accurately invert for a velocity profile, some corrections need to be applied to the *SS* and *S660S* stacks. Changes to the shapes of *S660S* and *SS* stacks arise from the surface crustal reflection and extra attenuation on *SS* (Shearer, 1996). To first order, the underside Moho reflection is positively polarized and arrives before the main *SS* arrival, whereas the topside reverberation off the Moho is negatively polarized and arrives after the *SS* arrival. The influence of oceanic crust on the long-period *SS* waveform is negligible due to its thinness, whereas thicker continental crust has a significant effect, deepening the sidelobe on the right side and elevating the sidelobe on the left side (Shearer, 1996). We construct a global oceanic stack by stacking all traces with midpoints located in regions where the crust is less than 10-km thick according to the CRUST1.0 model (Laske et al., 2013), and use this stack as a global reference *SS* phase. We convolve the reference phase with the crustal operator in each $1^\circ \times 1^\circ$ grid

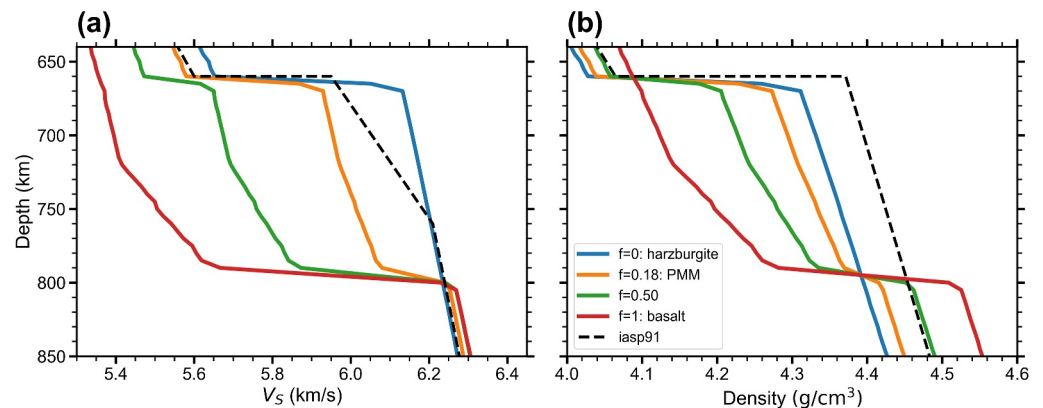


Figure 3. Velocity (a) and density (b) profiles of mechanical mixtures of basalt and harzburgite with various basalt fractions (f) along a normal geotherm (Katsura, 2022). PMM is the pyrolitic mechanical mixture (PMM), with a basalt fraction of 0.18. The profiles are calculated based on the mineral database of Stixrude and Lithgow-Bertelloni (2022) using the Perple_X package (Connolly, 2005).

based on the CRUST1.0 model, and the difference between the convoluted waveform and the reference is the crustal correction term. Finally, the average crustal correction term for each group stack is subtracted from the respective SS stack to correct for the crustal effect. The corrected SS stacks are nearly indistinguishable, particularly on the left side, suggesting appropriate crustal corrections (Figure 1e).

The extra attenuation of SS relative to $S660S$ reduces the amplitude of SS and widens its pulse. To correct for this attenuation effect, we convolve a t^* operator calculated from the PREM model (Dziewonski & Anderson, 1981) with $S660S$ stacks (Figure 1f) for comparison with SS pulses. Prior global studies also corrected for the effect of incoherent stacking of $S660S$ (e.g., Shearer, 1996; Yu et al., 2023). However, this correction is not applied in this study because all cap stacks are re-aligned to their maximum amplitude near the predicted arrival time before group stacking. Given that the long-period $S660S$ is only sensitive to large-scale structure (approximately 10°), the incoherent stacking effect within a single cap with a 5° radius is considered negligible.

The $S660S$ stacks after the attenuation correction exhibit significantly different characteristics (Figure 1f). Given that the right-side waveform is significantly affected by the 520- and 560-km discontinuities (Tian et al., 2020), and recognizing that depth resolution diminishes as one moves away from the 660-km depth, we restrict our analysis to the 40-s time window on the left side of the waveform, corresponding to depths of approximately 660–830 km. There is no prominent difference between neutral and slow stacks, whereas the fast stack features a lower peak, a shallower trough, and higher amplitude within the time window of -40 to -30 s, even when accounting for uncertainty. The difference in the $S660S$ waveform probably reflects distinctive velocity structure between subduction zones and other regions, which our inversion aims to explore.

2.3. Inversion of Velocity, Density, and Composition

With the corrected SS and $S660S$ stacks, we employ a Bayesian inversion algorithm to obtain V_S and density profiles, as well as the composition at and below the d660. As mentioned above, we focus on the waveform in the time window of 0–40 s before the $S660S$ peak. Similar to Bissig et al. (2023), we employ two parameterizations: seismic and thermodynamic (Figure 2). The seismic parameterization directly solves for a layered model of velocity and density, whereas the thermodynamic parameterization adjusts temperature and composition, which are then used to predict the velocity and density profiles. To parameterize composition, we assume a mechanical mixture model of harzburgite and basalt (Figure 3), with the basalt fraction ranging from 0% to 80%. The compositions of these endmembers in the $\text{Na}_2\text{O}-\text{CaO}-\text{FeO}-\text{MgO}-\text{Al}_2\text{O}_3-\text{SiO}_2$ chemical system are taken from Khan et al. (2009) (Table S1 in Supporting Information S1). For the two endmembers, the Perple_X package (Connolly, 2005) is used to conduct Gibbs' free energy minimization, and the bulk and shear moduli, as well as the density, are calculated based on the equations of state in Stixrude and Lithgow-Bertelloni (2022). The elastic moduli of the mixture are obtained by the Voigt-Reuss-Hill average (Hill, 1952) of the properties of the two endmembers, and the density is the weighted mean density based on their respective fractions. Therefore, given

any combination of temperature and basalt fraction, the velocity and density profiles are computed as intermediary models to fit the waveform.

Most 1D global reference models have a high-gradient layer just below the d660 and a low-gradient layer at greater depths (Dziewonski & Anderson, 1981; Kennett & Engdahl, 1991). Due to its long period, the *S660S* waveform is sensitive to these gradients, prompting us to assume three layers in both the seismic and thermodynamic parameterizations (Figure 2). The first layer is the d660 with a fixed width of 12 km, the global average thickness based on Lawrence and Shearer (2006). The d660 depth (d_{660}), the middle depth in this layer, is estimated by the average travel time deviations from the predicted arrival in the cap stacks. The *S660S* arrivals are 3 and 0 s earlier than the prediction in the fast and neutral stacks and 1 s later in the slow stack, corresponding to d660 depths of 671, 660, and 657 km, respectively (see details in Section 3.1). Figure S3 in Supporting Information S1 suggests that the middle depths of the velocity jump, representing d_{660} , are determined by the post-spinel transition in harzburgite and depend on the temperature rather than the basalt fraction. Therefore, d_{660} can be directly translated to the temperature at 660-km depth, which are 1850, 2050, and 2100 K for fast, neutral, and slow stacks, respectively. The temperature profile near the d660 is constructed assuming an adiabatic temperature gradient of 0.38 K/km near the d660 (Katsura, 2022). In contrast to the first layer, the boundaries of the second and third layers (d_1 and d_2) are free parameters in the inversion (Figure 2). Since the long-period *S660S* cannot distinguish between a narrow layer with an impedance jump and a thick layer with a steep gradient, we assume the thicknesses of the second and third layers to be at least 30 km. This assumption allows us to concentrate on impedance gradients rather than abrupt jumps below the d660. The velocity and density profiles at unspecified depths follow the IASP91 model. Note that the fixed thickness of d660 and the minimum thicknesses of the second and third layers are applied to reduce the long-period uncertainty and complexities in the inversion. Although some inversion parameters, particularly the boundary depths in seismic results, could be influenced by variations in these layer settings, the velocity and density gradients, which are primarily sensitive to the waveform amplitude, are well constrained.

The above model settings allow us to focus on waveform shapes, which are sensitive to relative changes in velocity and density instead of their absolute values. Based on the three-layer models, the velocity changes in the first and second layers (dv_1 and dv_2) are additional free parameters in the seismic parameterization, whereas the velocity change in the third layer depends on these free parameters (Figure 2). Velocities within layers are linearly interpolated. The density is scaled using $dV_S/d\rho = 1.644$, where 1.644 is the ratio of velocity to density changes between 660 and 800-km depths in the IASP91 model. In the thermodynamic parameterization, neither a velocity nor density profile is assumed. In addition to the boundaries of the three layers, the other free parameters are three basalt fractions: f_1 above and at the d660 layer, f_2 at the second boundary (d_1), and f_3 at the third boundary (d_2). The basalt fraction in the first layer does not change with depth, whereas those within the second and third layers are linearly interpolated to avoid abrupt compositional jumps at the boundaries. In summary, we have four free parameters in the seismic parameterization (d_1, d_2, dv_1, dv_2) and five parameters (d_1, d_2, f_1, f_2, f_3) in the thermodynamic parameterization (Figure 2).

The inverse problem is expressed as $\mathbf{d} = G(\mathbf{m})$, where \mathbf{d} is the corrected *S660S* waveform stack on the left side (0–40 s before the *S660S* arrival), \mathbf{m} contains the free parameters customizing the velocity and density profiles, and G is the forward waveform modeling operator. The Bayes' theorem can be formulated as follows:

$$p(\mathbf{m}|\mathbf{d}) \propto p(\mathbf{m})\mathcal{L}(\mathbf{d}|\mathbf{m}). \quad (1)$$

The prior knowledge $p(\mathbf{m})$ is modulated through the likelihood function $\mathcal{L}(\mathbf{d}|\mathbf{m})$ to reach the posterior probability density function $p(\mathbf{m}|\mathbf{d})$. We use an L2-norm likelihood function, which is expressed as

$$\mathcal{L}(\mathbf{d}|\mathbf{m}) \propto \exp(-\Phi), \quad (2)$$

and

$$\Phi = \frac{\|G(\mathbf{m}) - \mathbf{d}\|^2}{2\sigma^2}, \quad (3)$$

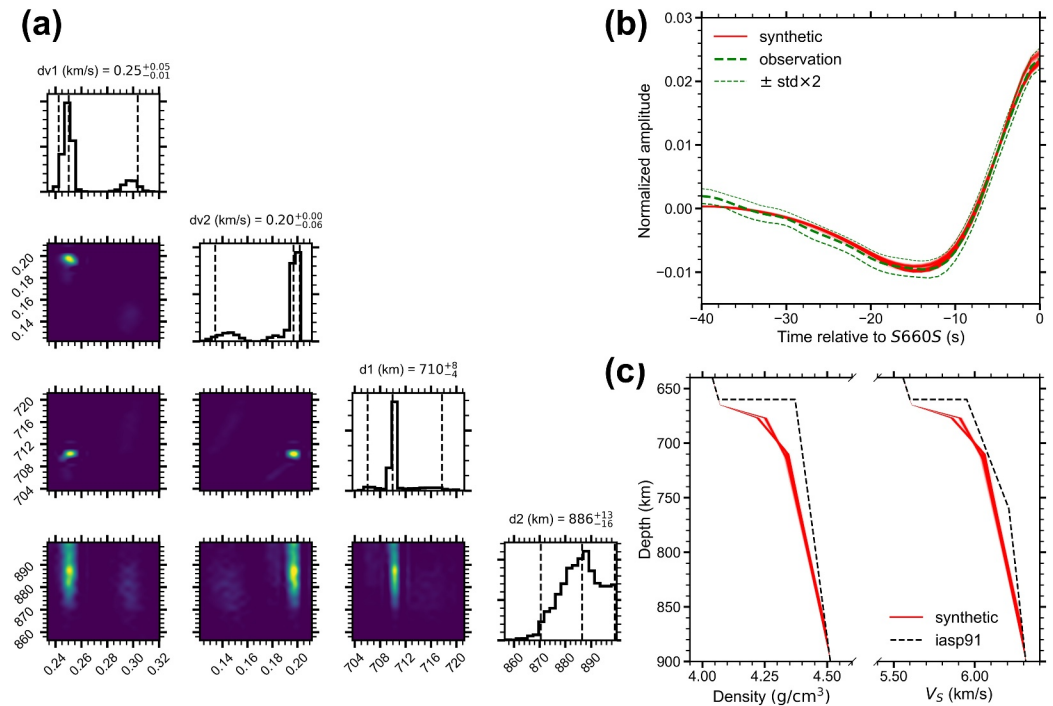


Figure 4. Inversion results for the fast stack in the seismic parameterization. (a) Corner plot of Bayesian samples. The dashed lines represent the 2.5%, 50%, and 97.5% quantiles, accompanied by corresponding values in subtitles. (b) Observed and synthetic $S660S$ stacks. The observation is shown as the average with two standard errors estimated by bootstrapping. The synthetics are generated from Bayesian samples. (c) V_s and density profiles based on the samples, in comparison with the IASP91 model (Kennett & Engdahl, 1991).

where σ is the standard deviation of the data vector \mathbf{d} , which is obtained by bootstrapping. We assume uniform prior distributions of all parameters within a relatively large range (Table S2 in Supporting Information S1). With the emcee python package (Foreman-Mackey et al., 2013), we implement the affine-invariant ensemble sampler for Markov chain Monte Carlo in our inversion. This method provides a reasonable criterion of convergence, that is, the number of steps should be more than 50 times the integrated autocorrelation time. With this criterion, we apply the method to three group stacks in two parameterizations with 24 walkers and 200,000 steps. The first 10% of the samples are discarded as the burn-in period, and every 10th sample is retained from the remaining samples to reduce autocorrelation. The distribution of samples with 200,000 steps is the same as that with 100,000 steps, further corroborating sufficient steps.

3. Results

The topography of the d660 and the peak amplitude of $S660S$ in caps containing more than 100 bounce points are shown in Figures 1c and 1d. Inversion results for the fast, neutral, and slow stacks in the seismic parameterization are presented in Figures 4, S4, and S5 in Supporting Information S1, respectively. Correspondingly, the inversion results in the thermodynamic parameterization are shown in Figures 5, S11, and S12 in Supporting Information S1. A comprehensive summary of all inversion results is presented in Figure 6, with the radial variations of basalt fraction shown in Figure 7.

3.1. Topography and Peak Amplitude of the d660

The topography of the d660 is directly estimated by the travel time deviations from the predicted $S660S$ arrival ($\Delta T = (t_{SS} - t_{660})_{obs} - (t_{SS} - t_{660})_{pred}$) in each cap. The conversion from travel time deviations to discontinuity depths requires that the ratio between the discontinuity depth deviation (Δd_{660}) and the travel time deviation (ΔT) does not change significantly with epicentral distance. Based on the IASP91 model (Kennett & Engdahl, 1991), $\Delta d_{660}/\Delta T$ is 4.14 km/s at 120° , 3.81 km/s at 140° , and 3.45 km/s at 170° . None of the travel time deviations in the three group stacks exceeds 3 s and the interpreted d660 depths for ΔT of 3 s are 12.42, 11.43, and

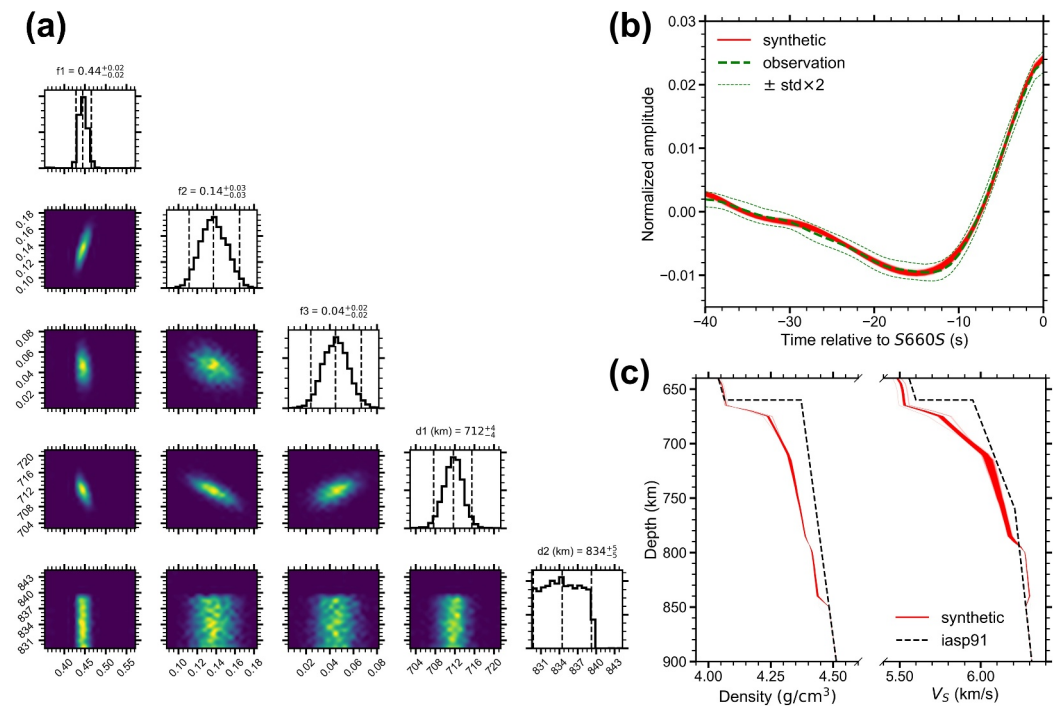


Figure 5. Inversion results for the fast stack in the thermodynamic parameterization. The subplots and line representations are analogous to those in Figure 4.

10.35 km at 120, 140, and 170°, respectively. Using $\Delta d_{660}/\Delta T$ of the average epicentral distance, 140°, the topography of the d660 can be estimated with an uncertainty of 1 km. Moreover, considering that the inversion depends on the waveform shapes rather than the topography (travel time), the small uncertainty in the topography does not affect the inversion.

Regions below the western Pacific, South America, and Tethys subduction zone exhibit a significantly depressed 660 (Figure 1c). An elevated d660 is observed in the Indian Ocean, northern Atlantic Ocean, and West Antarctica. The large-scale depressed and elevated d660s are generally consistent with the fast and slow regions in Figure 1b, suggesting cold subducted slabs and hot mantle upwelling, respectively. The large-scale pattern of the topography of the d660 also agrees with prior SS precursor studies (e.g., W. Wang, Xu, et al., 2020; Waszek et al., 2021), but the absolute depth perturbations vary, likely due to the different tomography models used to correct for velocity heterogeneity in the upper mantle. The peak amplitude of S660S (Figure 1d) exhibits a similar spatial pattern to that of the topography of the d660. On a large scale, the S660S amplitude is notably low in the western Pacific and South America, where deep subducting slabs are present.

3.2. Velocity/Density at and Below the d660

The distribution of Bayesian samples, corresponding synthetic waveforms, and velocity/density profiles in the seismic parameterization are shown in Figures 4, S4, S5, and S7 in Supporting Information S1. Notably, four parameters exhibit small uncertainty, which relies on both the small stacking error and priori model settings on the layer thickness. Due to the long period of S660S, the thicknesses of the three layers are poorly constrained. The thickness of the d660 is proportional to the impedance jump of the d660 if it is included as a free parameter in the inversion (Figure S8 in Supporting Information S1), but the average depth and velocity gradient in each layer are well resolved. The synthetic waveforms demonstrate close fits to all stacks except in the time window of −40 to −35 s in the fast stack (Figure 4). The poor fit is attributed to the higher amplitude in the fast stack compared with the other stacks (Figure 1f). This discrepancy is likely caused by anomalous structure near 800-km depth, such as the 810-km reflector produced by a subducted oceanic plateau located west of the Sea of Okhotsk (Wei et al., 2020). Such structure is not considered in the three-layer model settings. The synthetics and velocity

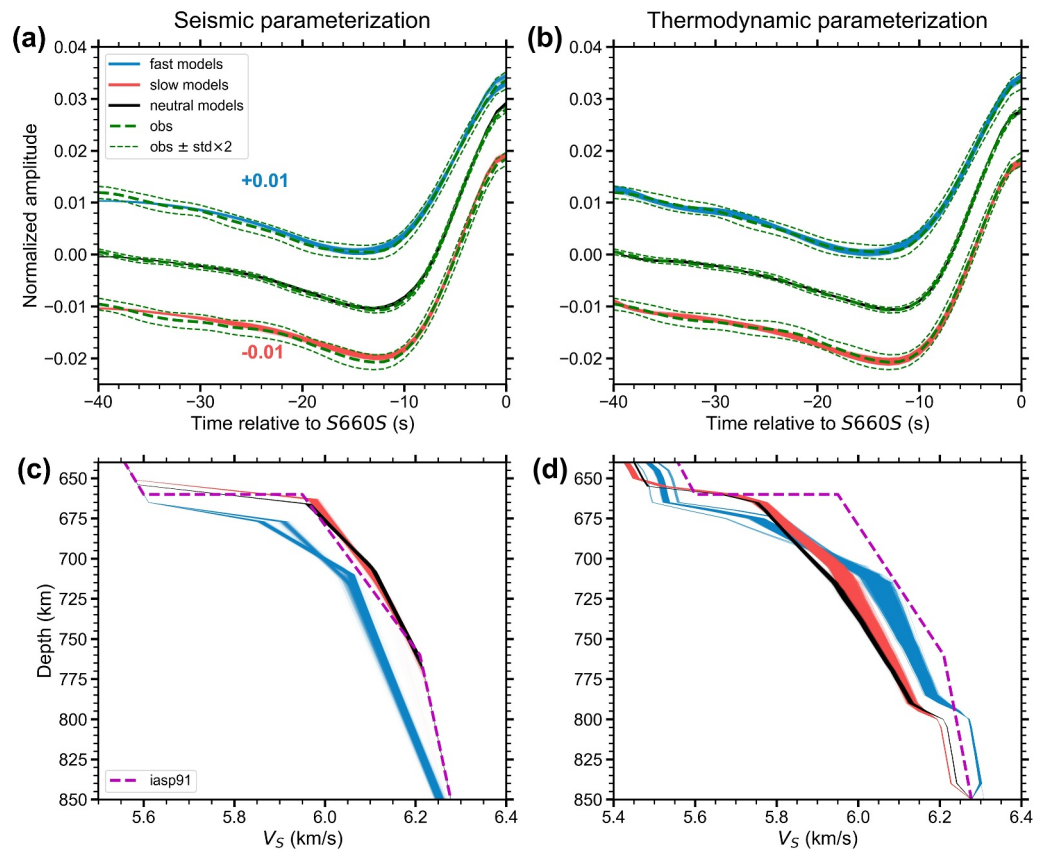


Figure 6. Summary of inversion results for the seismic (a, c) and thermodynamic parameterizations (b, d). (a, b) Synthetic left-side *S660S* waveforms calculated based on the Bayesian samples in three groups and their respective observations. Fast and slow models are shifted for better comparison. (c, d) Corresponding velocity profiles based on the samples in panels (a, b), respectively, in comparison with the IASP91 model.

profiles of Bayesian samples in three groups are summarized in Figures 6a and 6c, where the distribution of samples for the fast and slow stacks appears slightly broader, attributable to their larger stacking error (Figure 1f).

The inverted velocity profiles for the slow and neutral stacks are consistent with each other and align with the IASP91 model (Figures 6, S4, and S5 in Supporting Information S1), featuring a d660 jump and a steep gradient between the d660 and 760-km depth. In contrast, the velocity profiles for the fast stack exhibit a smaller d660 jump, a notably steep velocity gradient between the d660 and 710-km depth, and an underlying moderate-gradient layer (Figure 6c). The smaller d660 jump is anticipated because the fast stack has a lower *S660S* peak than other stacks (Figure 1f). Note that the waveform inversion is only sensitive to velocity changes, thus only the jumps and gradients, rather than absolute velocities, can be robustly compared. The lower absolute velocity/density of the fast profiles, compared to other profiles, result from the same reference velocity and density profiles above the d660 from the IASP91 model. Increasing the velocity/density by a small factor (e.g., 1.005) has a negligible effect on the waveform fitting (Figure S6 in Supporting Information S1).

Our approach employs a consistent scaling factor between velocity and density variations, resulting in density profiles that mirror the patterns observed in velocity profiles (Figures 4, S4, and S5 in Supporting Information S1). However, this consistency disagrees with 1D reference models like IASP91 and PREM, which typically feature two layers with distinct velocity gradients beneath the d660 but exhibit a single layer with a uniform density gradient. This discrepancy between velocity and density profiles contradicts common sense from mineral physics that the density gradient usually changes monotonously with the velocity gradient for a given composition. For example, calculations based on the *Perple_X* package show that the density gradients change with the velocity gradients synchronously for the basaltic, harzburgitic, and pyrolitic composition (Figure 3). The asynchronous behavior between density and velocity is caused by the relatively poor constraint on density in the lower

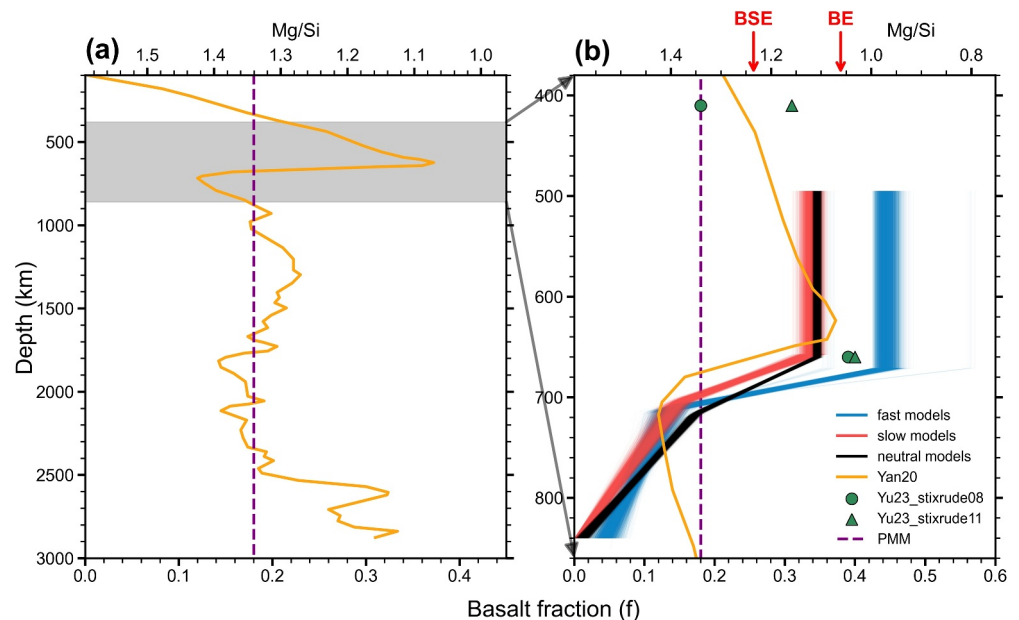


Figure 7. Radial variations of basalt fraction and Mg/Si ratio. (a) Radial variations of basalt fraction and Mg/Si ratio from geodynamic modeling of Yan et al. (2020). (b) A close-up radial variation of basalt content near the d660. The blue, red, and black lines are Bayesian inversion results for the three groups in this study. Results from Yan et al. (2020) and Yu et al. (2023) are plotted for comparison. There are two different mineral data sets (Stixrude & Lithgow-Bertelloni, 2011; Xu et al., 2008) used in Yu et al. (2023), labeled as “stixrude08” and “stixrude11.” Typical composition of the bulk Earth (BE), bulk silicate Earth (BSE), and the pyrolitic mechanical mixture (PMM) are from Allegre et al. (1995) and annotated by red arrows and a dashed line.

mantle in 1D models. In the PREM model, the velocities in the lower mantle are fitted with three different polynomials in three sub-regions, whereas the density is fitted using a single polynomial (Dziewonski & Anderson, 1981). Note that waveform fitting is sensitive to reflection coefficients, which depend on impedance contrasts rather than velocity contrasts only. Therefore, the inverted absolute velocity and density changes are significantly influenced by the scaling factor. These scaling factors are intricately linked with factors such as composition, temperature, and pressure, variables that are not explicitly captured in the seismic parameterization, whereas the thermodynamic parameterization can provide more stringent constraints. Nevertheless, the seismic results provide straightforward velocity and density profiles that better fit the waveforms. These profiles can be compared with the thermodynamic results for validation and better interpretation.

3.3. Radial Variations of Basalt Content at and Below the d660

Prior studies primarily have focused on fitting the travel time and peak amplitude of *S660S* using a constant basalt fraction without radial variations. However, such a configuration fails to adequately fit the entire waveform of *S660S* (Figures S9 and S10 in Supporting Information S1). In contrast, in this study, incorporating radial variations of basalt content achieves satisfactory fits for both the peak amplitude and the sidelobe of *S660S* (Figures 5, S11, and S12 in Supporting Information S1). The basalt fractions in the three layers in the thermodynamic parameterization exhibit robust sampling with small standard deviations (Figures 5, S11, and S12 in Supporting Information S1). In comparison to the synthetics in the seismic parameterization, those in the thermodynamic parameterization display broader distributions (Figure 6), but they still show a reasonable waveform fit with small residuals (Figures 5, S11, and S12 in Supporting Information S1). Similar to the results in the seismic parameterization, the inverted basalt fractions and corresponding velocity profiles for the neutral and slow stacks are in good agreement because of their similar waveforms (Figures 6 and 7). However, the results for the fast stack are significantly different.

Because of the post-spinel transition, harzburgite exhibits velocity and density jumps at the d660, whereas basalt does not (Figure 3). Therefore, a higher basalt fraction generates a lower d660 jump. Between the d660 and approximately 800-km depth, basalt exhibits lower velocity and density than harzburgite (Figure 3), thus

decreasing the basalt fraction substantially enhances the velocity gradient. At the d660 layer, the basalt fractions for the neutral and slow stacks are approximately 35%, with an uncertainty of 1%–2%, whereas that for the fast stack is $44 \pm 2\%$ (Figure 7). The higher basalt fraction leads to smaller velocity and density jumps, consistent with the seismic results (Figure 6). In the second layer, the basalt fractions for all stacks decrease rapidly to approximately 15%, resulting in significantly steep velocity gradients (Figures 6 and 7). The decrease of basalt fraction in the fast group is more significant than the others, so its velocity gradient in the second layer is steeper, consistent with the seismic results. In the third layer, the basalt fractions of all stacks decrease further to less than 10%, and the corresponding velocity gradients decrease to a level similar to that in the IASP91 model (Figures 6d and 7b). However, the *S660S* waveform in the time window of -40 to -30 s may be more affected by mid-mantle structures rather than the d660, and the *SS* waveform in this time window could be affected by the lithosphere–asthenosphere boundary. Therefore, the inversion results below approximately 800-km depth (corresponding to about -30 s) are more likely affected by other structures. Nevertheless, the basalt fraction between the d660 and 800-km depth remains consistently at a much lower level than that of the d660.

4. Discussion

Our results reveal a global basalt-enriched layer at the d660 (Figure 7), consistent with recent *SS* precursor studies (Bissig et al., 2023; Tauzin et al., 2022; Yu et al., 2023). The basalt fractions for three stacks are close to the global estimate of 40% by Yu et al. (2023). The accumulation of basalt at the d660 results from the density crossover between basalt and harzburgite: Basalt has a higher density than harzburgite above the d660 but a lower density at depths of about 660–800 km (Figure 3). In addition, the basalt fraction in subduction zones at the d660 layer is higher than other regions, which agrees with the results in Bissig et al. (2023) and Tauzin et al. (2022). The higher basalt fraction may be attributed to the segregation of oceanic crust from subducting slabs (e.g., Lee & Chen, 2007) or stagnating slabs in some regions, such as northwestern Pacific (e.g., Tao et al., 2018).

Moreover, our results reveal a global layer enriched in harzburgite right below the d660. The basalt fraction decreases from approximately 35%–44% at the d660 to less than 10% at 800-km depth. The harzburgite-rich layer also results from the density crossover between basalt and harzburgite because harzburgite is denser than basalt at depths of approximately 660–800 km but lighter at other depths (Figure 3). The basalt profile near the d660 in this study allows for a detailed assessment of the radial variations of basalt fraction and corresponding Mg/Si ratio in the mantle in combination with prior findings (Figure 7). The velocities and density in the upper mantle above the MTZ can be fit with a pyrolytic composition (e.g., Irifune et al., 2008; Zhao et al., 2022), characterized by a Mg/Si ratio of approximately 1.3, but this ratio notably decreases to about 1.1 at the d660 (Yu et al., 2023). However, according to our results, there is a substantial decrease in basalt fraction at depths between 660 and 800 km, leading to a notable increase in the Mg/Si ratio from approximately 1.1 to 1.5 (Figure 7). This change corresponds to a chemical transition from a chondrite-like composition, which typically represents the average composition of the bulk Earth (Allegre et al., 1995), to one that is significantly silica-poor (Figure 7). At greater depths, prior studies agree on a silica-rich lower mantle, characterized by a Mg/Si ratio of approximately 1.1 (e.g., Deng et al., 2023; Mashino et al., 2020; Murakami et al., 2012), close to the chondritic composition (Allegre et al., 1995).

The significant variations of basalt content near the d660 observed in this study corroborate the prediction of geodynamic modeling (Yan et al., 2020) and the substantial compositional layering is also supported by significant short-scale topography of the d660 in some regions (Wu et al., 2019). The pronounced radial compositional variations in the mantle challenge the applicability of a radial homogeneous model, such as the pyrolite model, in the MTZ and the lower mantle. Furthermore, the significantly silica-poor layer below the d660 may have a considerable effect on the viscosity and thus the dynamics between the upper and lower mantle, affecting the behaviors of subducting slabs and upwelling plumes, which warrants further investigation.

It is worth noting that the absolute velocity and density calculated in thermodynamic modeling depend on mineral databases, and uncertainty in these databases may introduce biases in constraining composition with absolute velocity/density profiles. However, relative changes in mineral properties are generally more robust than absolute values, enhancing the reliability of our method in constraining composition (Cammarano et al., 2003). Despite this advantage, the discrepancy between mineral databases still requires further investigation to resolve. It would be ideal to achieve consistent results of composition and temperature with seismic observations from absolute (e.g., tomography models) and relative (e.g., discontinuity studies) velocity/density values. Additionally, the

mechanical mixture model in this study does not account for other effects, such as the presence of water in the MTZ. A ubiquitous high water content in the MTZ significantly reduces absolute velocities, making it unable to fit the travel times (Yu et al., 2023). A small amount of water, for example, 0.2 wt% (W. Wang et al., 2021), may not have a substantial effect on the absolute velocities, but it still slightly decreases the velocity above the d660 and thereby increases the impedance contrast across the d660 (Yu et al., 2023). Consequently, a higher basalt content than our modeling results is required to match the observed low impedance contrasts of the d660. The water content could be anomalously high, resulting in partial melting below the d660 in some regions, particularly in subduction zones (Schmandt et al., 2014; X. Wang, Chen, et al., 2020), providing an alternative mechanism for the low impedance contrast. However, partial melting induced by water or other volatiles below the d660 is unlikely a global feature, thus not contradicting our large-scale results. Furthermore, since there is no significant change in water content below the d660, the effect of water on impedance change is negligible, ensuring the robustness of our conclusion regarding a harzburgite-enriched layer.

5. Conclusion

Within a Bayesian framework, *S660S* waveforms are fit with layered seismic and thermodynamic models in subduction zones and other regions. Seismic results in subduction zones exhibit a smaller d660 jump and a steeper gradient than other regions, whereas other regions have profiles consistent with 1D reference models. Thermodynamic results show a significant decrease in basalt fraction with depth, suggesting a global basalt-enriched layer at the d660 and a global harzburgite-enriched layer below it. Subduction zones are more enriched in basalt at the d660 compared to other regions, resulting in velocity profiles consistent with the seismic results. Detailed radial profiles of the basalt fraction and corresponding Mg/Si ratio in the mantle are obtained by integrating our results with prior interdisciplinary studies. Our results provide a robust constraint on global compositional layering between the upper and lower mantle, with the silica-poor layer in the uppermost lower mantle potentially exerting a significant influence on mantle dynamics.

Conflict of Interest

The authors declare no conflicts of interest relevant to this study.

Data Availability Statement

We use 1987–2018 data from the following seismic networks (abbreviations defined at www.fdsn.org/networks/): AC, AE, AF, AI, AK, AT, AU, AV, BE, BL, BX, C1, CB, CD, CH, CM, CN, CT, CU, CZ, DK, DR, DW, EI, G, GB, GE, GT, HL, HT, IC, II, IP, IU, JP, KN, KO, KP, KR, KS, KZ, LX, MC, MI, MM, MS, MX, MY, NA, ND, NJ, NO, NR, NU, OE, OV, PL, PM, PR, PS, RM, RV, S, SV, TA, TM, TR, TT, TW, UK, US, VE, WI, and WM. All raw seismic data are available at the Data Management Center of Incorporated Research Institutions for Seismology (<http://ds.iris.edu/ds/nodes/dmc/>). We also use 1995–2018 F-net data set (<https://doi.org/10.17598/nied.0005>) from Japan's National Research Institute for Earth Science and Disaster Resilience (National Research Institute for Earth Science and Disaster Resilience, 2019).

References

- Allegre, C. J., Poirier, J.-P., Humler, E., & Hofmann, A. W. (1995). The chemical composition of the Earth. *Earth and Planetary Science Letters*, 134(3–4), 515–526. [https://doi.org/10.1016/0012-821x\(95\)00123-t](https://doi.org/10.1016/0012-821x(95)00123-t)
- Bissig, F., Khan, A., & Giardini, D. (2023). Joint inversion of PP and SS precursor waveforms and Rayleigh wave phase velocities for global mantle transition zone structure. *Geophysical Journal International*, 233(1), 316–337. <https://doi.org/10.1093/gji/ggac451>
- Cammarano, F., Goes, S., Vacher, P., & Giardini, D. (2003). Inferring upper-mantle temperatures from seismic velocities. *Physics of the Earth and Planetary Interiors*, 138(3–4), 197–222. [https://doi.org/10.1016/s0031-9201\(03\)00156-0](https://doi.org/10.1016/s0031-9201(03)00156-0)
- Connolly, J. A. (2005). Computation of phase equilibria by linear programming: A tool for geodynamic modeling and its application to subduction zone decarbonation. *Earth and Planetary Science Letters*, 236(1–2), 524–541. <https://doi.org/10.1016/j.epsl.2005.04.033>
- Deng, X., Xu, Y., Hao, S., Ruan, Y., Zhao, Y., Wang, W., et al. (2023). Compositional and thermal state of the lower mantle from joint 3D inversion with seismic tomography and mineral elasticity. *Proceedings of the National Academy of Sciences*, 120(26), e2220178120. <https://doi.org/10.1073/pnas.2220178120>
- Dziewonski, A. M., & Anderson, D. L. (1981). Preliminary reference Earth model. *Physics of the Earth and Planetary Interiors*, 25(4), 297–356. [https://doi.org/10.1016/0031-9201\(81\)90046-7](https://doi.org/10.1016/0031-9201(81)90046-7)
- Efron, B., & Tibshirani, R. (1991). Statistical data analysis in the computer age. *Science*, 253(5018), 390–395. <https://doi.org/10.1126/science.253.5018.390>
- Farber, D. L., Williams, Q., & Ryerson, F. J. (1994). Diffusion in Mg₂SiO₄ polymorphs and chemical heterogeneity in the mantle transition zone. *Nature*, 371(6499), 693–695. <https://doi.org/10.1038/371693a0>

Acknowledgments

S.H. and P.M.S. were supported by NSF Grant EAR-2123529. S.S.W. was supported by the MSU Geological Endowment. We thank Dr. Lars Stixrude for constructive discussions. We are grateful to Dr. Chunquan Yu and three anonymous reviewers for their detailed and constructive reviews which greatly improved the manuscript.

- Foreman-Mackey, D., Hogg, D. W., Lang, D., & Goodman, J. (2013). emcee: The MCMC hammer. *PASP*, 125(925), 306–312. <https://doi.org/10.1086/670067>
- Hill, R. (1952). The elastic behaviour of a crystalline aggregate. *Proceedings of the Physical Society Section A*, 65(5), 349–354. <https://doi.org/10.1088/0370-1298/65/5/307>
- Hirose, K., Fei, Y., Ma, Y., & Mao, H.-K. (1999). The fate of subducted basaltic crust in the Earth's lower mantle. *Nature*, 397(6714), 53–56. <https://doi.org/10.1038/16225>
- Hofmann, A., & Hart, S. (1978). An assessment of local and regional isotopic equilibrium in the mantle. *Earth and Planetary Science Letters*, 38(1), 44–62. [https://doi.org/10.1016/0012-821x\(78\)90125-5](https://doi.org/10.1016/0012-821x(78)90125-5)
- Hosseini, K., Matthews, K. J., Sigloch, K., Shephard, G. E., Domeier, M., & Tsekhmistrenko, M. (2018). Submachine: Web-based tools for exploring seismic tomography and other models of Earth's deep interior. *Geochemistry, Geophysics, Geosystems*, 19(5), 1464–1483. <https://doi.org/10.1029/2018gc007431>
- Irifune, T., Higo, Y., Inoue, T., Kono, Y., Ohfuji, H., & Funakoshi, K. (2008). Sound velocities of majorite garnet and the composition of the mantle transition region. *Nature*, 451(7180), 814–817. <https://doi.org/10.1038/nature06551>
- Ishii, T., Kojitani, H., & Akaogi, M. (2019). Phase relations of harzburgite and MORB up to the uppermost lower mantle conditions: Precise comparison with pyrolite by multisample cell high-pressure experiments with implication to dynamics of subducted slabs. *Journal of Geophysical Research: Solid Earth*, 124(4), 3491–3507. <https://doi.org/10.1029/2018jb016749>
- Katsura, T. (2022). A revised adiabatic temperature profile for the mantle. *Journal of Geophysical Research: Solid Earth*, 127(2), e2021JB023562. <https://doi.org/10.1029/2021jb023562>
- Kennett, B., & Engdahl, E. (1991). Traveltimes for global earthquake location and phase identification. *Geophysical Journal International*, 105(2), 429–465. <https://doi.org/10.1111/j.1365-246x.1991.tb06724.x>
- Khan, A., Boschi, L., & Connolly, J. (2009). On mantle chemical and thermal heterogeneities and anisotropy as mapped by inversion of global surface wave data. *Journal of Geophysical Research: Solid Earth*, 114(B9). <https://doi.org/10.1029/2009jb006399>
- Laske, G., Masters, G., Ma, Z., & Pasyanos, M. (2013). Update on CRUST1.0—A 1-degree global model of Earth's crust. *Geophysical Research Abstracts*, 15, 2658.
- Lawrence, J. F., & Shearer, P. M. (2006). Constraining seismic velocity and density for the mantle transition zone with reflected and transmitted waveforms. *Geochemistry, Geophysics, Geosystems*, 7(10). <https://doi.org/10.1029/2006gc001339>
- Lee, C.-T. A., & Chen, W.-P. (2007). Possible density segregation of subducted oceanic lithosphere along a weak serpentinite layer and implications for compositional stratification of the Earth's mantle. *Earth and Planetary Science Letters*, 255(3–4), 357–366. <https://doi.org/10.1016/j.epsl.2006.12.022>
- Lei, W., Ruan, Y., Bozdağ, E., Peter, D., Lefebvre, M., Komatitsch, D., et al. (2020). Global adjoint tomography—Model GLAD-M25. *Geophysical Journal International*, 223(1), 1–21. <https://doi.org/10.1093/gji/ggaa253>
- Maguire, R., Ritsema, J., & Goes, S. (2017). Signals of 660 km topography and harzburgite enrichment in seismic images of whole-mantle upwellings. *Geophysical Research Letters*, 44(8), 3600–3607. <https://doi.org/10.1002/2017gl073120>
- Mashino, I., Murakami, M., Miyajima, N., & Petitgirard, S. (2020). Experimental evidence for silica-enriched Earth's lower mantle with ferrous iron dominant bridgmanite. *Proceedings of the National Academy of Sciences*, 117(45), 27899–27905. <https://doi.org/10.1073/pnas.1917096117>
- Murakami, M., Ohishi, Y., Hirao, N., & Hirose, K. (2012). A perovskitic lower mantle inferred from high-pressure, high-temperature sound velocity data. *Nature*, 485(7396), 90–94. <https://doi.org/10.1038/nature11004>
- National Research Institute for Earth Science and Disaster Resilience. (2019). F-net dataset. <https://doi.org/10.17598/nied.0005>
- Ringwood, A. (1962). A model for the upper mantle. *Journal of Geophysical Research*, 67(2), 857–867. <https://doi.org/10.1029/jz067i002p00857>
- Schmandt, B., Jacobsen, S. D., Becker, T. W., Liu, Z., & Dueker, K. G. (2014). Dehydration melting at the top of the lower mantle. *Science*, 344(6189), 1265–1268. <https://doi.org/10.1126/science.1253358>
- Shearer, P. M. (1993). Global mapping of upper mantle reflectors from long-period SS precursors. *Geophysical Journal International*, 115(3), 878–904. <https://doi.org/10.1111/j.1365-246x.1993.tb01499.x>
- Shearer, P. M. (1996). Transition zone velocity gradients and the 520-km discontinuity. *Journal of Geophysical Research: Solid Earth*, 101(B2), 3053–3066. <https://doi.org/10.1029/95jb02812>
- Shephard, G. E., Matthews, K. J., Hosseini, K., & Domeier, M. (2017). On the consistency of seismically imaged lower mantle slabs. *Scientific Reports*, 7(1), 10976. <https://doi.org/10.1038/s41598-017-11039-w>
- Stixrude, L., & Lithgow-Bertelloni, C. (2011). Thermodynamics of mantle minerals-II. Phase equilibria. *Geophysical Journal International*, 184(3), 1180–1213. <https://doi.org/10.1111/j.1365-246x.2010.04890.x>
- Stixrude, L., & Lithgow-Bertelloni, C. (2012). Geophysics of chemical heterogeneity in the mantle. *Annual Review of Earth and Planetary Sciences*, 40(1), 569–595. <https://doi.org/10.1146/annurev.earth.36.031207.124244>
- Stixrude, L., & Lithgow-Bertelloni, C. (2022). Thermal expansivity, heat capacity and bulk modulus of the mantle. *Geophysical Journal International*, 228(2), 1119–1149. <https://doi.org/10.1093/gji/ggab394>
- Tao, K., Grand, S. P., & Niu, F. (2018). Seismic structure of the upper mantle beneath eastern Asia from full waveform seismic tomography. *Geochemistry, Geophysics, Geosystems*, 19(8), 2732–2763. <https://doi.org/10.1029/2018gc007460>
- Tauzin, B., Waszek, L., Ballmer, M. D., Afonso, J. C., & Bodin, T. (2022). Basaltic reservoirs in the Earth's mantle transition zone. *Proceedings of the National Academy of Sciences*, 119(48), e2209399119. <https://doi.org/10.1073/pnas.2209399119>
- Tian, D., Lv, M., Wei, S. S., Dorfman, S. M., & Shearer, P. M. (2020). Global variations of Earth's 520- and 560-km discontinuities. *Earth and Planetary Science Letters*, 552, 116600. <https://doi.org/10.1016/j.epsl.2020.116600>
- Van Keken, P., Karato, S., & Yuen, D. (1996). Rheological control of oceanic crust separation in the transition zone. *Geophysical Research Letters*, 23(14), 1821–1824. <https://doi.org/10.1029/96gl01594>
- Wang, W., Xu, Y., Sun, D., Ni, S., Wentzcovitch, R., & Wu, Z. (2020b). Velocity and density characteristics of subducted oceanic crust and the origin of lower-mantle heterogeneities. *Nature Communications*, 11(1), 64. <https://doi.org/10.1038/s41467-019-13720-2>
- Wang, W., Zhang, H., Brodholt, J. P., & Wu, Z. (2021). Elasticity of hydrous ringwoodite at mantle conditions: Implication for water distribution in the lowermost mantle transition zone. *Earth and Planetary Science Letters*, 554, 116626. <https://doi.org/10.1016/j.epsl.2020.116626>
- Wang, X., Chen, Q.-F., Niu, F., Wei, S., Ning, J., Li, J., et al. (2020a). Distinct slab interfaces imaged within the mantle transition zone. *Nature Geoscience*, 13(12), 822–827. <https://doi.org/10.1038/s41561-020-00653-5>
- Waszek, L., Tauzin, B., Schmerr, N. C., Ballmer, M. D., & Afonso, J. C. (2021). A poorly mixed mantle transition zone and its thermal state inferred from seismic waves. *Nature Geoscience*, 14(12), 949–955. <https://doi.org/10.1038/s41561-021-00850-w>
- Wei, S. S., & Shearer, P. M. (2017). A sporadic low-velocity layer atop the 410 km discontinuity beneath the Pacific Ocean. *Journal of Geophysical Research: Solid Earth*, 122(7), 5144–5159. <https://doi.org/10.1002/2017jb014100>

- Wei, S. S., Shearer, P. M., Lithgow-Bertelloni, C., Stixrude, L., & Tian, D. (2020). Oceanic plateau of the Hawaiian mantle plume head subducted to the uppermost lower mantle. *Science*, 370(6519), 983–987. <https://doi.org/10.1126/science.abd0312>
- Wu, W., Ni, S., & Irving, J. C. (2019). Inferring Earth's discontinuous chemical layering from the 660-kilometer boundary topography. *Science*, 363(6428), 736–740. <https://doi.org/10.1126/science.aav0822>
- Xu, W., Lithgow-Bertelloni, C., Stixrude, L., & Ritsema, J. (2008). The effect of bulk composition and temperature on mantle seismic structure. *Earth and Planetary Science Letters*, 275(1–2), 70–79. <https://doi.org/10.1016/j.epsl.2008.08.012>
- Yamazaki, D., Kato, T., Yurimoto, H., Ohtani, E., & Toriumi, M. (2000). Silicon self-diffusion in MgSiO₃ perovskite at 25 GPa. *Physics of the Earth and Planetary Interiors*, 119(3–4), 299–309. [https://doi.org/10.1016/s0031-9201\(00\)00135-7](https://doi.org/10.1016/s0031-9201(00)00135-7)
- Yan, J., Ballmer, M. D., & Tackley, P. J. (2020). The evolution and distribution of recycled oceanic crust in the Earth's mantle: Insight from geodynamic models. *Earth and Planetary Science Letters*, 537, 116171. <https://doi.org/10.1016/j.epsl.2020.116171>
- Yu, C., Goes, S., Day, E. A., & van der Hilst, R. D. (2023). Seismic evidence for global basalt accumulation in the mantle transition zone. *Science Advances*, 9(22), eadg0095. <https://doi.org/10.1126/sciadv.adg0095>
- Zhao, Y., Wu, Z., Hao, S., Wang, W., Deng, X., & Song, J. (2022). Elastic properties of Fe-bearing akimotoite at mantle conditions: Implications for composition and temperature in lower mantle transition zone. *Fundamental Research*, 2(4), 570–577. <https://doi.org/10.1016/j.fmre.2021.12.013>